JPET Fast Forward. Published on December 4, 2020 as DOI: 10.1124/jpet.120.000385
This article has not been copyedited and formatted. The final version may differ from this version.

Physiologically-Based Pharmacokinetics of Lysosomotropic Chloroquine in Rat and Man

Xin Liu and William J. Jusko

Department of Pharmaceutical Sciences, School of Pharmacy and Pharmaceutical Sciences, State University of New York at Buffalo, Buffalo, New York

JPET Fast Forward. Published on December 4, 2020 as DOI: 10.1124/jpet.120.000385
This article has not been copyedited and formatted. The final version may differ from this version.

Running Title: PBPK Modeling of Chloroquine

Corresponding Author: William J. Jusko, Ph.D., Department of Pharmaceutical Sciences, School of Pharmacy and Pharmaceutical Sciences, 404 Pharmacy Building, State University of New York at Buffalo, Buffalo, NY, 14214, E-mail: wjjusko@buffalo.edu

Number of text pages: 22 (including Abstract)

Number of tables: 4

Number of figures: 7

Number of references: 60

Number of words:

Abstract: 249

Introduction: 742

Discussion: 1527

ABBREVIATIONS: *GFR*, Glomerular Filtration Rate; IC_{50}, drug concentration causing 50% inhibition; NCA, Non-compartmental analysis; PBPK, physiologically-based pharmacokinetic.

Recommended Section: Metabolism, Transport, and Pharmacogenetics

JPET Fast Forward. Published on December 4, 2020 as DOI: 10.1124/jpet.120.000385
This article has not been copyedited and formatted. The final version may differ from this version.

ABSTRACT

A semi-mechanistic physiologically-based pharmacokinetic (PBPK) model for chloroquine (CQ), a highly lysosomotropic weak base, was applied to digitized rat (Adelusi and Salako, 1982a) and human (Frisk-Holmberg et al, 1984) concentration versus time data. The PBPK model in rat featured plasma and RBC concentrations, extensive and apparent nonlinear tissue distribution, fitted hepatic and renal intrinsic clearances, and a plasma half-life of about 1 day. Tissue to plasma CQ ratios at 50 h after dosing were highest in lung, kidney, liver, and spleen (182-318) and lower in heart, muscle, brain, eye, and skin (11-66). The RBC to plasma ratio of 11.6 was assumed to reflect cell lipid partitioning. A lysosome-based extended model was used to calculate subcellular CQ concentrations based on tissue mass balances, fitted plasma, interstitial, and free cytosol concentrations, and literature-based pH and pKa values. The CQ tissue component concentrations ranked: lysosome >> acidic phospholipid > plasma = interstitial = cytosol ≥ neutral lipids. The extensive lysosome sequestration appeared to change over time and was attributed to lowering pH values caused by proton pump influx of hydrogen ions. The man-to-rat volume of distribution (*Vss*) ratio of 7 used to scale rat tissue partitioning to man along with estimation of hepatic clearance allowed excellent fitting of oral dose PK (150-600 mg) of CQ with a 50-day half-life in man. The prolonged PK of chloroquine was well-characterized for rat and man with this PBPK model. The calculated intra-tissue concentrations and lysosomal effects have therapeutic relevance for CQ and other cationic drugs.

JPET Fast Forward. Published on December 4, 2020 as DOI: 10.1124/jpet.120.000385
This article has not been copyedited and formatted. The final version may differ from this version.

Significance Statement:

Sequestration in lysosomes is a major factor controlling the pharmacokinetics and pharmacology of chloroquine and other cationic drugs. This report provides comprehensive physiologic modeling of chloroquine distribution in tissues and overall disposition in rat and man revealing expected complexities and inferences related to its subcellular association with various tissue components.

JPET Fast Forward. Published on December 4, 2020 as DOI: 10.1124/jpet.120.000385
This article has not been copyedited and formatted. The final version may differ from this version.

Introduction

Chloroquine (CQ) is a classic anti-malarial agent that was identified in 1934, approved by the FDA in 1949, and features additional immunomodulatory, anti-viral, anti-cancer, and neurological activities (Savarino et al, 2002; Plantone and Koudriavtseva, 2018; Schrezenmeier and Dorner, 2020). The general pharmacological and pharmacokinetic (PK) properties of this 4-aminoquinoline compound are shared by hydroxychloroquine (HCQ) and several newer compounds (White, 1985).

The clinical pharmacokinetics of CQ have been extensively reviewed (White, 1985; Ducharme and Farinotti, 1996). In man, the drug is well-absorbed after oral doses of 150 to 600 mg, exhibits modest plasma protein binding (fraction unbound, *fu* is 0.40) (Walker et al, 1983), undergoes partial renal excretion with 70% of an oral dose excreted unchanged in urine, is partly metabolized by CYP2C8 and CYP3A4/5 enzymes to de-ethylated metabolites (McChesney et al., 1966, Kim, et al, 2003), and is enantiomeric with modest differences in disposition of its R- and S-forms. The mono-desethyl metabolite is also active. Most notable is its extensive tissue distribution having a steady-state volume of distribution (*Vss*) of about 800 L/kg and terminal half-life ($t_{1/2}$) of 30 to 60 days in man (Frisk-Holmberg et al, 1984; Moore et al, 2011). The strong tissue affinity and large *Vss* of CQ is attributed to lysosomal trapping of this lipophilic cation along with association with acidic phospholipids in cell membranes.

While there is little experimental data for CQ distribution in human tissues, there is extensive evidence for CQ distribution into various tissues of rats. Lysosomal uptake of CQ has been directly studied (Allison and Young, 1964; MacIntyre and Cutler, 1988, 1993; Tietz et al, 1990; Daniel et al, 1995; Zhang et al, 2011). The drug has often been used as a positive control for assessing lysosomal function and uptake of other moderate-to-strong bases (Cramb, 1986;

JPET Fast Forward. Published on December 4, 2020 as DOI: 10.1124/jpet.120.000385
This article has not been copyedited and formatted. The final version may differ from this version.

Myers et al, 1995; Ishizaki et al, 2000). The overall distribution of CQ into 10 tissues of rats over time was described (Adalusi and Salako, 1982a), but the data have not been analyzed by physiologically-based PK (PBPK) modeling. On the other hand, more limited tissue data for HCQ in rats was subjected to PBPK (Collins et al, 2018).

While it has long been recognized that lipophilic bases exhibit strong tissue binding and relatively large *Vss* values (Watanabi and Kozaki, 1978), it was not until 2002 that a PBPK perspective offered a tissue compositional concept for these drugs depicting the joint roles of ionization, lipid partitioning, pH differentials, and lysosomal trapping of ionized cations (Yokogawa et al, 2002). These ideas were later extended to consider diffusive movement of drug molecules within cell compartments (Trapp et al, 2008; Zheng et al, 2011). A more complete tissue composition-based model for such compounds was evolved (Assmus et al, 2017).

Software for operation of generic PBPK models (SimulationsPlus, SimCyp, PK-Sim) include general methods for estimating tissue-to-plasma partition coefficients (K_p) of various drugs based on chemical nature (acid, base, neutral), physicochemical properties (logP, pKa), the *fu* of the drug, and the partial tissue composition. Prediction methods for moderate-to-strong lipophilic bases include the lipid composition of various tissues (Rodgers et al, 2005). Such predictions are considered good when tissue-plasma ratios fall within 3-fold of known values. This approach was extended to include lysosomal trapping in lysosome-rich organs such as liver, kidney, and lung (Assmus et al, 2017). While compounds considered included propranolol and imipramine that are known (Cramb, 1986; Ishizaki et al, 2000) to trap in lysosomes of rats, none of the 9 antimalarial agents in clinical use (White, 1985; Trapp et al, 2008) were included. CQ differ from many others in being a divalent rather than monovalent base. Equations for K_p that include lysosomal trapping in some tissues are in the current SimulationsPlus (Lancaster, CA)

JPET Fast Forward. Published on December 4, 2020 as DOI: 10.1124/jpet.120.000385
This article has not been copyedited and formatted. The final version may differ from this version.

software.

With the extensive pre-clinical and human PK data available for CQ and the absence of detailed modeling, it is of interest to apply PBPK modeling to explore how the extensive lysosomal trapping explains in vivo PK. This report: 1.) Applies a generalized PBPK model to digitized data for CQ in various tissues of rats (Adelusi and Salako, 1982a); 2.) Scales the PBPK model to digitized data for CQ PK in man (Frisk-Holmberg et al, 1984); 3.) Adapts published equations (Rodgers et al, 2005; Assmus et al, 2017) for calculating tissue drug concentrations with lysosomal trapping; 4.) Considers the relevance of lysosomotropic effects of CQ (lysosomal changes in pH, volume, and lipids) on its PK; and 5.) Relates these assessments to the pharmacology of CQ and related compounds.

Materials and Methods

Data Analysis

The CQ concentration versus time data for plasma and tissues of rats (Adelusi and Salako 1982a), and blood CQ concentration versus time for man (Frisk-Holmberg et al, 1984) were obtained by digitization (Rodiovov, 2000). The blood from rats was obtained by cardiac puncture. Blood concentrations for man were converted to plasma concentrations using the authors' published relationship. The numerical data used are listed in Tables S1 and S2 in the Supplemental Materials.

Measured tissue CQ concentration ($C_{t(meas)}$) data of rat were corrected for assumed residual blood by first converting measured red blood cell (RBC) to plasma (C_{pl}) concentration ratios (K_b) to whole blood concentrations (C_{bl}):

$$C_{bl} = C_{pl} \cdot (1 + (K_b - 1) \cdot Hct) \quad (1)$$

JPET Fast Forward. Published on December 4, 2020 as DOI: 10.1124/jpet.120.000385
This article has not been copyedited and formatted. The final version may differ from this version.

The hematocrit (*Hct*) value of rat used was 0.4 (Lee and Blaufox, 1985). Then adjustments to the corrected tissue concentrations (C_t) were made using:

$$C_t = \frac{C_{t(meas)} - C_{bl} \cdot (V_{vasc}/V_t)}{1-(V_{vasc}/V_t)} \quad (2)$$

where V_{vasc} and V_t are tissue vascular and total tissue volumes. Literature values for V_{vasc} were from (Bernareggi and Rowland, 1991).

Tissue partition coefficients *Kp* were obtained by parameter estimation through PBPK modeling as described in detail below. In addition, in silico *Kp* predictions were obtained for comparison using GastroPlus™ PBPK Simulator (version 9.6.2, Simulations Plus Inc., Lancaster, CA) based on published methods (Poulin and Theil, 2002), (Berezhkovskiy, 2004), (Rodgers and Rowland, 2006) and an adapted method (Assmus et al, 2017) in the software that includes lysosomal trapping for basic compounds.

PBPK Model

Figure 1 shows the proposed general PBPK model structure for CQ. This model consists of red blood cells (RBC), plasma, liver, kidney, lung, spleen, heart, brain, muscle, skin, eye and a remainder compartment. The elimination pathway for CQ is partly hepatic metabolism and partly renal clearance in rodents. Only CQ in plasma (not RBC) was assumed to access tissue spaces. The renal clearance for CQ consisting of glomerular filtration (*GFR*) and active secretion was fixed to two times *GFR*. Physiological parameter definitions and values are listed in Table 1 and 2. Plasma flow and tissue volumes were obtained from (Brown et al, 1997; Bernareggi and Rowland, 1991).

A nonlinear total cytosol (*TC*) to cytosol water partition coefficient for CQ (Kp_{tissue}) was applied due to variable concentration ratios between tissues and plasma. It was assumed that only the free fraction of CQ from the interstitial space (*IS*) was available to cytosol and available for

JPET Fast Forward. Published on December 4, 2020 as DOI: 10.1124/jpet.120.000385
This article has not been copyedited and formatted. The final version may differ from this version.

apparent binding:

$$Kp_{tissue,u} = 1 + \frac{B_{max}}{C_{IS}+K_D} \quad (3)$$

where C_{IS} is the free concentration of CQ in interstitial space, B_{max} is the binding capacity for different tissues (μg/ml), and K_D is the equilibrium dissociation constant (μg/ml). A different K_D *(K_{D2})* was applied for skin (Olatunde, 1971), eye and muscle due to melanin binding of CQ in skin and eye and because muscle has a similar curve shape as skin.

The differential equations for various compartments of the PBPK model are:

Artery:

$$V_{artery} \cdot \frac{dC_{artery}}{dt} = Input1 + Q_{lung} \cdot \frac{C_{lung.IS}}{fu} - (Q_{liver} + Q_{kidney} + Q_{heart} + Q_{muscle} + Q_{skin} + Q_{spleen} + Q_{brain} + Q_{eye} + Q_{rest}) \cdot C_{artery} - fu \cdot GFR \cdot C_{artery} \quad (4)$$

Vein:

$$V_{vein} \cdot \frac{dC_{vein}}{dt} = (Q_{liver} + Q_{spleen}) \cdot \frac{C_{liver.IS}}{fu} + Q_{kidney} \cdot \frac{C_{kidney.IS}}{fu} + Q_{heart} \cdot \frac{C_{heart,IS}}{fu} + Q_{muscle} \cdot \frac{C_{muscle,IS}}{fu} + Q_{skin} \cdot \frac{C_{skin,IS}}{fu} + Q_{brain} \cdot \frac{C_{brain,IS}}{fu} + Q_{eye} \cdot \frac{C_{eye}}{Kp_{eye}} + Q_{rest} \cdot \frac{C_{rest}}{Kp_{rest}} - Q_{lung} \cdot C_{vein} \quad (5)$$

Liver:

$$V_{liver,IS} \cdot \frac{dC_{liver,IS}}{dt} = Input2 + Q_{liver} \cdot (C_{artery} - \frac{C_{liver,IS}}{fu}) + Q_{spleen} \cdot (\frac{C_{spleen,IS}}{fu} - \frac{C_{liver,IS}}{fu}) - PS_1 \cdot (C_{liver,IS} - \frac{C_{liver,TC}}{Kp_{u,liver}}) \quad (6)$$

$$V_{liver,TC} \cdot \frac{dC_{liver,TC}}{dt} = PS_1 \cdot \left(C_{liver,IS} - \frac{C_{liver,TC}}{Kp_{u,liver}}\right) - CL_{u,int} \cdot \frac{C_{liver,TC}}{Kp_{u,liver}} \quad (7)$$

Kidney:

$$V_{kidney,IS} \cdot \frac{dC_{kidney.IS}}{dt} = Q_{kidney} \cdot \left(C_{artery} - \frac{C_{kidney,IS}}{fu}\right) - PS_2 \cdot \left(C_{kidney,IS} - \frac{C_{kidney,TC}}{Kp_{u,kidney}}\right) \quad (8)$$

$$V_{kidney,TC} \cdot \frac{dC_{kidney,TC}}{dt} = PS_2 \cdot \left(C_{kidney,IS} - \frac{C_{kidney,TC}}{Kp_{u,kidney}}\right) - CL_{k,int} \cdot \frac{C_{kidney,TC}}{Kp_{u,kidney}} \quad (9)$$

JPET Fast Forward. Published on December 4, 2020 as DOI: 10.1124/jpet.120.000385
This article has not been copyedited and formatted. The final version may differ from this version.

Heart:

$$V_{heart,IS} \cdot \frac{dC_{heart,IS}}{dt} = Q_{heart} \cdot \left(C_{artery} - \frac{C_{heart,IS}}{fu}\right) - PS_3 \cdot \left(C_{heart,IS} - \frac{C_{heart,TC}}{Kp_{u,heart}}\right) \quad (10)$$

$$V_{heart,TC} \cdot \frac{dC_{heart,TC}}{dt} = PS_3 \cdot \left(C_{heart,IS} - \frac{C_{heart,TC}}{Kp_{u,heart}}\right) \quad (11)$$

Lung:

$$V_{lung,IS} \cdot \frac{dC_{lung,IS}}{dt} = Q_{lung} \cdot \left(C_{vein} - \frac{C_{lung,IS}}{fu}\right) - PS_2 \cdot \left(C_{lung,IS} - \frac{C_{lung,TC}}{Kp_{u,lung}}\right) \quad (12)$$

$$V_{lung,TC} \cdot \frac{dC_{lung,TC}}{dt} = PS_2 \cdot \left(C_{lung,IS} - \frac{C_{lung,TC}}{Kp_{u,lung}}\right) \quad (13)$$

Spleen:

$$V_{spleen,IS} \cdot \frac{dC_{spleen,IS}}{dt} = Q_{spleen} \cdot \left(C_{artery} - \frac{C_{spleen,IS}}{fu}\right) - PS_2 \cdot \left(C_{spleen,IS} - \frac{C_{spleen,TC}}{Kp_{u,spleen}}\right) \quad (14)$$

$$V_{spleen,TC} \cdot \frac{dC_{spleen,TC}}{dt} = PS_2 \cdot \left(C_{spleen,IS} - \frac{C_{spleen,TC}}{Kp_{u,spleen}}\right) \quad (15)$$

Brain:

$$V_{brain,IS} \cdot \frac{dC_{brain,IS}}{dt} = Q_{brain} \cdot \left(C_{artery} - \frac{C_{brain,IS}}{fu}\right) - PS_3 \cdot \left(C_{brain,IS} - \frac{C_{brain,TC}}{Kp_{u,brain}}\right) \quad (16)$$

$$V_{brain,TC} \cdot \frac{dC_{brain,TC}}{dt} = PS_3 \cdot \left(C_{brain,IS} - \frac{C_{brain,TC}}{Kp_{u,brain}}\right) \quad (17)$$

Muscle:

$$V_{muscle,IS} \cdot \frac{dC_{muscle,IS}}{dt} = Q_{muscle} \cdot \left(C_{artery} - \frac{C_{muscle,IS}}{fu}\right) - PS_4 \cdot \left(C_{muscle,IS} - \frac{C_{muscle,TC}}{Kp_{u,muscle}}\right) \quad (18)$$

$$V_{muscle,TC} \cdot \frac{dC_{muscle,TC}}{dt} = PS_4 \cdot \left(C_{muscle,IS} - \frac{C_{muscle,TC}}{Kp_{u,muscle}}\right) \quad (19)$$

Skin:

$$V_{skin,IS} \cdot \frac{dC_{skin,IS}}{dt} = Q_{skin} \cdot \left(C_{artery} - \frac{C_{skin,IS}}{fu}\right) - PS_4 \cdot \left(C_{skin,IS} - \frac{C_{skin,TC}}{Kp_{u,skin}}\right) \quad (20)$$

$$V_{skin,TC} \cdot \frac{dC_{skin,TC}}{dt} = PS_4 \cdot \left(C_{skin,IS} - \frac{C_{skin,TC}}{Kp_{u,skin}}\right) \quad (21)$$

JPET Fast Forward. Published on December 4, 2020 as DOI: 10.1124/jpet.120.000385
This article has not been copyedited and formatted. The final version may differ from this version.

Eye:

$$V_{eye} \cdot \frac{dC_{eye}}{dt} = Q_{eye} \cdot \left(C_{artery} - \frac{C_{eye}}{Kp_{eye}}\right) \quad (22)$$

Remainder:

$$V_{rest} \cdot \frac{dC_{rest}}{dt} = Q_{rest} \cdot \left(C_{artery} - \frac{C_{rest}}{Kp_{rest}}\right) \quad (23)$$

where interstitial volume ($V_{i,IS}$), intracellular volume ($V_{i,TC}$), IS concentration ($C_{i,IS}$) TC concentration ($C_{i,TC}$), plasma flow (Q_i) and partition coefficients ($Kp_{u,i}$) are applied for tissue *i*; $CL_{u,int}$ and $CL_{k,int}$ are the unbound intrinsic clearances in liver and kidney; and $PS_{1\text{-}4}$ are the permeability coefficients between interstitial and cell spaces. Assuming 1 g/mL tissue density: V_{rest} = body weight – summation of volumes for listed tissues, plasma and RBC; Q_{rest} = cardiac plasma output - summation of plasma flows for listed tissues.

The CQ concentrations in RBC and plasma were related as the partition coefficient (K_b):

$$C_{RBC} = K_b \cdot C_{plasma} \quad (24)$$

The dosing input for intraperitoneal (*IP*) dosing of CQ in rats was:

$$\frac{dA_{IP}}{dt} = -\left(ka_{plasma} \cdot fd \cdot A_{IP} + ka_{liver} \cdot (1 - fd) \cdot A_{IP}\right) \qquad A_{IP}(0) = Dose \quad (25)$$

$$Input1 = ka_{plasma} \cdot fd \cdot A_{IP} \quad (26)$$

$$Input2 = ka_{liver} \cdot (1 - fd) \cdot A_{IP} \quad (27)$$

where *fd* is the dose fraction directly entering plasma that was fixed to 0.1.

For human data, the systemic renal clearance ($CL_{s,kidney}$) was set as 70% of total systemic clearance ($CL_{s,total}$) calculated based on non-compartmental analysis (NCA) of the plasma data and intrinsic hepatic clearance ($CL_{u,int}$) was fitted. The connectivity of systemic ($CL_{s,total}$) and intrinsic clearances was assessed using:

$$CL_{s,total} = Q_{liver} \cdot \frac{fu \cdot CL_{u,int}}{Q_{liver} + fu \cdot CL_{u,int}} + Q_{kidney} \cdot \frac{fu \cdot CL_{k,int}}{Q_{kidney} + fu \cdot CL_{k,int}} + fu \cdot GFR \quad (28)$$

JPET Fast Forward. Published on December 4, 2020 as DOI: 10.1124/jpet.120.000385
This article has not been copyedited and formatted. The final version may differ from this version.

The oral dosing input of CQ in humans in place of *Input2* in Eq. 6 is:

$$Input = ka_{plasma} \cdot A_{PO} \qquad A_{PO}(0) = F \cdot Dose \tag{29}$$

where the bioavailability (*F*) of CQ was assumed to be 1.0 (Frisk-Holmberg et al, 1984) and free fraction of plasma (*fu*) for man is 0.4 (Ducharme and Farinotti, 1996).

The initial conditions for all differential equations are equal to 0 except for the dosing sites.

Extended Lysosome Model

The lysosome model (Figure 2) was adapted from (Assmus et al, 2017, Rodgers et al, 2005) and based on assumptions that: (1) only neutral molecules diffuse through the lysosome membrane; (2) IS and cytosol concentrations are in *PS*-determined equilibrium with plasma concentrations; (3) neutral drug equilibrium occurs between lysosome and cytosol concentrations; (4) plasma and IS pH = 7.4, cytosol pH = 7.0, initial lysosome pH= 4.6, and lysosome pH= 5 at 10 h; (5) only neutral molecules bind to neutral lipids (NL) and neutral phospholipids (NP) while ionized drug binds to acidic phospholipids (AP).

The equations for the extended lysosome model are based on the mass balance:

$$C_{tissue} = f_{lyso} \cdot C_{lyso} + f_{cyto} \cdot C_{cyto} + f_{IS} \cdot C_{IS} + f_{NL} \cdot C_{NL} + f_{NP} \cdot C_{NP} + f_{AP} \cdot C_{AP} \tag{30}$$

where C_{tissue} *and* C_{IS} are total tissue and interstitial CQ concentrations fitted using the PBPK model, C_{lyso}, C_{cyto}, C_{NL}, C_{NP}, and C_{AP} are CQ concentrations associated with lysosomes, cytosol, neutral lipids, neutral phospholipids, and acidic phospholipids, while *fi* are volume fractions of total tissue for corresponding components. The following approach was applied for each tissue as adapted from (Assmus et al, 2017) with assigned parameters from (Rodgers et al, 2005):

The C_{cyto} are calculated from the fitted C_{TC} profiles using the partition coefficients:

$$C_{cyto} = \frac{C_{TC}}{Kp_{\,u,tissue}} \tag{31}$$

The C_{NL} and C_{NP} concentrations are calculated using the published *n*-octanol-to-water

JPET Fast Forward. Published on December 4, 2020 as DOI: 10.1124/jpet.120.000385
This article has not been copyedited and formatted. The final version may differ from this version.

partition coefficient (LogP = 4.63) (Lullmann and Wehling, 1979).

$$C_{NL} = C_{cyto} \cdot P \cdot Fn_{cyto} \quad (32)$$

$$C_{NP} = C_{cyto} \cdot (0.3 \cdot P + 0.7) \cdot Fn_{cyto} \quad (33)$$

where Fn_i are neutral CQ fractions in cytosol calculated from the known pKa values for the divalent CQ (Trapp et al, 2008):

$$Fn_i = \frac{C_{i,neutral}}{C_{i,total}} = (1 + 10^{pKa1-pH_i} + 10^{pKa1+pKa2-2\cdot pH_i})^{-1} \quad (34)$$

where *i* is either plasma, lysosome or cytosol.

The C_{AP} concentrations of CQ were calculated using the association constant (*Kap*):

$$C_{AP} = Kap \cdot AP \cdot C_{cyto} \cdot (1 - Fn_{cyto}) \quad (35)$$

where *AP* are tissue concentrations of acidic phospholipids and *Kap* was calculated from the $Kp_{u,RBC}$ using (Rodgers et al, 2005):

$$Kap = \frac{Kp_{u,RBC} - \frac{f_{cyto}\cdot Fn_{PL}}{Fn_{cyto}} - \left(P\cdot f_{nl} + (0.3\cdot P + 0.7)\cdot f_{np}\right)\cdot Fn_{PL}}{AP\cdot\left(\frac{1}{Fn_{cyto}} - 1\right)\cdot Fn_{PL}} \quad (36)$$

where $Kp_{u,RBC} = K_b/fu = 29$ and *fu* is the free fraction of drug in plasma.

The CQ concentrations in lysosomes in relation to C_{cyto} are governed by equilibration of the neutral molecules and pH-partitioning:

$$C_{lyso} = C_{cyto} \cdot \frac{Fn_{cyto}}{Fn_{lyso}} \quad (37)$$

It was assumed that the pH of lysosome is 5 at 10 h for all tissues. With initial substitution of $f_{AP} = (1 - f_{NL} - f_{IS} - f_{NP} - f_{cyto} - f_{lyso})$, Eq. 30 was re-arranged to calculate the effective volume fraction f_{lyso} for all tissues using:

$$f_{lyso} = \frac{C_{tissue} - C_{cyto}\cdot f_{cyto} - C_{IS}\cdot f_{IS} - C_{NP}\cdot f_{NP} - C_{NL}\cdot f_{NL} - \left(1 - f_{NL} - f_{IS} - f_{NP} - f_{cyto}\right)\cdot C_{AP}}{C_{lyso} - C_{AP}} \quad (38)$$

where C_{tissue} are total CQ tissue concentrations fitted with the PBPK model. Then, assuming f_{lyso}

JPET Fast Forward. Published on December 4, 2020 as DOI: 10.1124/jpet.120.000385
This article has not been copyedited and formatted. The final version may differ from this version.

is constant, the pH of lysosomes for each time point was calculated using:

$$C_{lyso} = \frac{C_{tissue} - C_{cyto} \cdot f_{cyto} - C_{IS} \cdot f_{IS} - C_{NL} \cdot f_{NL} - C_{NP} \cdot f_{NP} - (1 - f_{lyso} - f_{NL} - f_{IS} - f_{NP} - f_{cyto}) \cdot C_{AP}}{f_{lyso}} \quad (39)$$

$$Fn_{lyso} = C_{cyto} \cdot \frac{Fn_{cyto}}{C_{lyso}} \quad (40)$$

$$pH = log\left(\frac{-10^{pKa1} - \sqrt{(10^{pKa1})^2 - 4 * \left(1 - \frac{1}{Fn_{lyso}}\right) * 10^{pKa1+pKa2}}}{2 * \left(1 - \frac{1}{Fn_{lyso}}\right)}\right) \quad (41)$$

where Eq. 41 was derived by re-arranging Eq. 34.

The modeling was performed in stages. First, Eq. 3 – 27 were applied to fit the rat PBPK plasma and tissue data and generate C_{tissue}, C_{IS} and C_{TC} concentrations over time. This assumes that the nonlinear tissue binding reflects overall lipid partitioning and lysosomal trapping of CQ. Then, the lysosome model (Eq. 30-39) was used to calculate the theoretical lipid and lysosome concentrations of CQ followed by generation of apparent pH values over time for each tissue (Eq. 39-41). Subsequently, the PBPK model was applied to fit the human PK data. Lastly, the tissue subcomponent model was applied to the human PK using literature values for lipid components in man (Rogers et al, 2005).

Model Fitting

For rat data, estimated were: binding capacity (B_{max}) and equilibrium dissociation constants (K_{D1} and K_{D2}) comprising the apparent partition coefficients (Kp) for all tissues, permeability coefficients (PS_{1-4}), two CQ absorption rate constants (ka_{plasma} and ka_{liver}), and the hepatic intrinsic clearance ($CL_{u,int}$). For human data, ka_{plasma}, $K_{D1,}$ and intrinsic hepatic clearance ($CL_{u,int}$) were estimated. All fittings and simulations were implemented using ADAPT 5 (Biomedical Simulations Resource, University of Southern California, Los Angeles, CA) using maximum likelihood estimation. The model was evaluated based on visual inspection of the

JPET Fast Forward. Published on December 4, 2020 as DOI: 10.1124/jpet.120.000385
This article has not been copyedited and formatted. The final version may differ from this version.

fitted profiles and CV% of parameter estimates. The variance model was: $V_i = (\sigma_1 + \sigma_2 \cdot Y_i)^2$ where V_i represents the variance of the ith data point, Y_i is the ith model prediction, and σ_1 and σ_2 are variance model parameters. Figures were created using GraphPad Prism 8.42 (GraphPad Software, La Jolla, CA). The PBPK model code is provided in the Supplemental Materials.

Results

Whole-body pharmacokinetics of CQ for rat

Figure 3 shows the measured CQ concentration in plasma and tissues from (Adelusi and Salako, 1982a) along with the PBPK model-fitted time-course profiles after single IP dosing. The highest drug concentrations are found in liver, lung, spleen and kidney. Heart, brain, and eye had intermediate concentrations and the others were much lower. The plasma and RBC concentrations were parallel, which supported use of a linear K_b constant. Generally, the PBPK model captures the plasma, RBC, and tissue PK very well. Blood in rats was obtained by cardiac punctures and thus was a mixture of arterial and venous blood. It was necessary to assume that this represented arterial concentrations, but use of mixed venous blood concentrations is commonplace in many PBPK models. The sampling site is only likely to make a difference for drugs with much more rapid distribution kinetics than CQ (Huang and Isoherranen, 2020).

The fitted parameters for each tissue obtained from model-fitting are listed in Table 2. Most parameters were estimated with good precision as indicated by the CV% values. The tissue-to-plasma ratios and *Kp* values for all tissues exceed 1.0 after the absorption/distribution phase and varies among the tissues. The tissue-to-plasma ratios increase over time, but at 50-h are 318 for liver, 275 for lung, 267 for spleen, 182 for kidney, and 66 for heart, indicating extensive distribution of CQ. The B_{max} and K_D account for the variable *Kp* values that create the

JPET Fast Forward. Published on December 4, 2020 as DOI: 10.1124/jpet.120.000385
This article has not been copyedited and formatted. The final version may differ from this version.

non-parallel decline of tissue versus plasma concentrations and produce higher tissue to plasma ratios as time progresses (Table 2). The B_{max} values were specific for each tissue, but two groups of K_D values provided good fittings across the array of tissues. These were optimized by trial-and-error seeking the most parsimonious sets of parameters. The tissues with the highest CQ concentrations had the higher B_{max} values as expected. The permeability component of the model was applied to all tissues except eye and remainder; the inclusion of $PS_{1\text{-}4}$ significantly improved the up-curve shapes of all organs at the early time periods compared to fittings without this parameter. These up-curves varied somewhat and optimal fittings were obtained by using four different *PS* values with liver exhibiting the highest PS value and brain the lowest as expected (Jeong et al, 2017). The K_{D2} values were associated with the tissues with the least CQ uptake.

For optimal fittings, it was necessary to separate the IP dosing into two routes, 90% into liver and 10% into plasma with 100% bioavailability, so two different *ka* values were applied, slower into liver and faster into plasma. It seemed reasonable that a small part of the dose could be absorbed systemically. Renal clearance consisting of passive filtration ($f_u \cdot GFR$) and active transport along with hepatic clearance ($CL_{u,int}$) are responsible for CQ clearance. The systemic renal clearance (630 mL/h/kg) was fixed to 2 times *GFR* (Grundmann et al, 1972). The *GFR* was handled as direct removal from arterial plasma (Eq. 4) as the very high kidney concentrations complicated its attachment to Eq. 8. The model-estimated hepatic intrinsic clearance was 11,600 mL/h/kg and exhibited the highest CV% (70.3) of all parameters. All other values were less than 36%. Based on systemic clearances obtained using Eq. 28, the kidney accounts for 29.7% of CQ disposition and the liver 70.3%, in agreement with findings that 26- 47% of the dose was excreted unchanged in urine of rats (Grundmann et al, 1972).

JPET Fast Forward. Published on December 4, 2020 as DOI: 10.1124/jpet.120.000385
This article has not been copyedited and formatted. The final version may differ from this version.

Table 2 lists the tissue-to-plasma ratios of CQ at times 10, 50, and 150 h to demonstrate the range of values as well as their time-dependence. The table also lists expected *Kp* values using three methods that do not include lysosomal uptake and one that does (Method 4). Methods 1-3 that include lipid binding as the major factor predict the early tissue-to-plasma ratios of CQ reasonably well only for those tissues with low lysosomal content. Method 4, which includes lysosomal uptake, reasonably predicts CQ values in most tissues except for muscle and skin. Methods such as Eq. 32 -36 are theoretical based on reasonable physiologic and physicochemical principles and the measured composition of tissues. However, they are very general and supported only by use of predictions of tissue-to-plasma ratios (*Kp*) of a variety of drugs (Rodgers et al, 2005; Assmus et al, 2017). Agreement between measured and predicted *Kp* values with such equations is inexact, usually within 2- or 3-fold as occurs with the results in Table 2. Direct in vivo measurement of drug associated with subcellular components requires imaging, which is difficult with whole tissues, and for drugs that are neither labeled nor fluoresce.

The basic PBPK model for CQ relies on digitized plasma concentrations and calculated tissue-to-plasma ratios (Adalusi and Salako, 1982a) and are thus close but inexact. However, the PBPK model-predicted descriptors of these concentrations such as *Cmax*, *Tmax*, and half-life are in reasonable concordance with the published values (see Supplemental Materials).

Extended lysosome model of CQ for rat

Figure 2 shows the structure of the multi-component lysosome model based on (Assmus et al, 2017) that was applied to the CQ tissue data. Table 3 lists the parameters and sources that were employed in Eq. 32-39 to calculate the subcellular concentrations of CQ. It was necessary to assume a pH of 5.0 at 10 h leading to a starting and eventual steady-state lysosomal pH of 4.6 for all tissues. It is cautioned that there could be a range of pH values in lysosomes distributed in

cells and among various tissues (Schmitt et al, 2019). Figure 4 shows calculated lysosome, cytosol, IS, neutral lipid, neutral phospholipid, and acidic phospholipid CQ concentration versus time profiles in all of the 8 tissues except eye along with the corresponding measured tissue concentrations. The lysosome concentrations are far higher than all others as governed by the pH gradient between lysosomes and cytosol. There is markedly greater ionization of CQ at the lower pH as indicated by the lower *Fn* values in Table 3. The acid phospholipids (AP) as governed by the *Kap* of 8.52 g/mg and high degree of ionization of CQ have the next highest CQ concentrations. The NL and NP concentrations of CQ are very low in spite of the relatively high logP of 4.63 owing to their access to only the neutral form of CQ for which the *Fn* is extremely low. The free drug in plasma, IS concentrations, and cytosol water concentrations are generally similar as these are equilibrating entities in the PBPK model. The cytosol and IS concentrations overlap in all tissues except liver and kidney where the cytosol concentrations are lower because of the clearance processes.

Figure 5 shows the calculated pH values in lysosomes in various tissues over time. It is assumed that the lysosome pH starts at a low value before CQ dosing, initially rises to higher values owing to influx of CQ, and slowly returns toward a baseline value of 4.6 with influx of hydrogen ions by the proton pump mechanism (Ishizaki et al, 2000; Ishida et al, 2013). This diminishment in lysosomal pH over time causing more uptake of CQ is the model-assigned reason for the increasing tissue-to-plasma ratios of CQ (Table 2).

An additional set of plasma and tissue data for CQ in rats (Adalusi and Salako, 1982b) was used to evaluate predictability of the basic PBPK model. Good concordance was found as shown in the Supplementary Materials.

Pharmacokinetics of CQ in man

JPET Fast Forward. Published on December 4, 2020 as DOI: 10.1124/jpet.120.000385
This article has not been copyedited and formatted. The final version may differ from this version.

The human PBPK model employed physiological parameters for man (Table 1), adjusted partition coefficients (from Table 2) based on the man-to-rat V_{ss} ratio, and fitted values of hepatic intrinsic clearance ($CL_{u,int}$), dissociation constant (K_{D1}) and ka_{plasm} (Table 4). Figure 6 shows excellent fittings of the 150, 300, 600 mg doses of CQ over the full time-course and parameter CV% values were very small. Oral absorption was relatively rapid producing the early high CQ concentrations.

The noncompartmental V_{ss} for man is 7 times that of rat, averaging 820 L/kg in man (Frisk-Holmberg et al, 1984) and (our calculated) 113 L/kg in rat (Adelusi and Salako, 1982a); thus we set *R* equal to 7.0 as an adjustment factor for multiplying rat *Kp* values. It was reported that 70% unchanged CQ is excreted by kidney in man (McChesney et al, 1966); hence the $CL_{s,kidney}$ was fixed to 70% of $CL_{s,total}$ that was estimated using NCA, and $CL_{u,int}$ was estimated by fitting the human data. The $CL_{u,int}$ is 1060 mL/h/kg, which results in $CL_{s,total}$ (722 ml/h/kg) similar to a reported value (Fisk-Holmberg et al, 1984).

Figure 7 shows the model-predicted CQ concentrations associated with all of the tissue components for four major tissues in man after the 600 mg dose. These were calculated based on published lipid contents for man (Table 3), but rat lysosomal fractions were employed. While the rank order of concentrations appears similar to those in rats (Figure 4), lysosomal concentrations were relatively higher in man. For example, in man lysosome-to-plasma CQ ratios at 1000 h were: 25054 for liver, 39654 for kidney, 56608 for lung, and 208976 for muscle. Corresponding values for rat at 50 h were: 3380, 8110, 8160, and 8530.

Discussion

Justification of the PBPK Model

JPET Fast Forward. Published on December 4, 2020 as DOI: 10.1124/jpet.120.000385
This article has not been copyedited and formatted. The final version may differ from this version.

The properties of chloroquine (CQ) are well-appreciated as it has been in clinical use since the 1950's and is a frequent probe for lysosomal functioning. Comprehensive reviews of its PK and pharmacology are available (White, 1985; Browning, 2014). The plasma and whole blood PK of CQ have been studied in several species and clearances were shown to scale allometrically (Moore et al, 2011).

The avid uptake of CQ into the liver, kidney, spleen, and lungs, which have abundant lysosomes, and lesser distribution to muscle and other tissues has been well-appreciated from other studies in rats (McChesney et al, 1965, 1967; Grundmann et al, 1972; Osifo, 1980), but the present data provide the most comprehensive view of the overall PK and tissue distribution of CQ in any species. The present PBPK modeling utilizes a two-stage approach, first generally assessing the array of 10 tissues and blood with classical PBPK modeling concepts, including apparent nonlinear tissue distribution. This provided estimates of CQ concentrations in IS and cell cytosol with the nonlinear component assumed to reflect CQ concentrations associated with various lipids and lysosomes. A complex distribution model for lipid binding and lysosome distribution (Assmus et al, 2017) was then adapted to allocate the total tissue concentrations of CQ into its subcomponents.

There is considerable evidence for lysosomal tissue distribution of CQ in rats supporting our PBPK modeling. The fluorescence of CQ facilitated early viewing of its high concentrations in intracellular lysosomes of cells (Allison and Young, 1964). Differential centrifugation and electrophoresis methods allowed measurement of the slow uptake of CQ into the hepatic lysosomes of rats dosed with CQ along with its inhibition of phospholipase A (Hostetler et al, 1985). Isolated rat hepatocytes demonstrated both uptake and metabolism of CQ, including marked reduction of uptake by ammonium chloride, a lysosomal inhibitor that alters lysosomal

JPET Fast Forward. Published on December 4, 2020 as DOI: 10.1124/jpet.120.000385
This article has not been copyedited and formatted. The final version may differ from this version.

pH (MacIntyre and Cutler, 1993). Their application of a cellular PK model argued that the permeability of the lysosomal membrane is rate limiting for hepatocyte uptake of CQ. A more complex model (similar to Figure 2) for the lysosomal uptake of CQ was developed for cells in culture (Trapp et al, 2008; Zheng et al, 2011). This process is mimicked by the simpler diffusion step (*PS*) between IS and cell content applied in our PBPK model (Figure 1) to account for the slow early rise in CQ concentrations in many tissues (Figure 3). The in vitro binding of CQ to various individual polar phospholipids has been measured (Lullmann and Wehling, 1979). The apparent partition coefficient of CQ for phosphotidylcholine was about 77 consistent with our AP-to-plasma ratios, and a *Kap* of about 2.0 g/mg, near to our *Kap* of 8.52 g/mg. Such in vitro binding was nonlinear for CQ and other compounds studied.

The nonlinear *Kp* in our basic PBPK model was used initially to account for the increases in tissue- to-plasma concentrations of CQ over time (Figure 3, Table 2). This may actually reflect a time-dependent process. Part of the lysosomotropic effects of CQ is the inhibition of phospholipid degradation (Hostetler et al, 1985). Use of isolated hepatocytes showed that acute exposure to CQ produces an increased lysosomal pH attributed to proton consumption (Tietz et al, 1990; Myers et al, 1995). Imaging of canine kidney cells has demonstrated phospholipidosis accompanied by altered vesicular pH and increased vesicle volume (Zhang et al, 2011). Our modeling (Figure 5) assumed that CQ produced, within hours of dosing, a rise in lysosome pH that slowly returned to the baseline owing to both elimination of CQ and influx of H^+ ions by the proton pump mechanism responsible for maintaining the normal low pH of 4 to 5. It is possible that phospholipodosis and increased vesicle volume also contribute to changing tissue-to-plasma ratios after CQ dosing (Table 2).

JPET Fast Forward. Published on December 4, 2020 as DOI: 10.1124/jpet.120.000385
This article has not been copyedited and formatted. The final version may differ from this version.

CQ exhibits strong binding to melanin, particularly in the eye (Schroeder and Gerber, 2014). This is implicated in ocular toxicity. The rat eye has modest concentrations of CQ (Figure 3, Table 2) and a small B_{max}. Melanin binding is saturable in vitro and the eye accounts for a very small fraction of CQ in the body.

The present effort was partly inspired by a publication describing the PBPK modeling of HCQ using data obtained from mice, many similar stated concepts, and with extrapolation to man (Collins et al, 2018). However, their modeling is based on only 4 tissues (blood, liver, kidney, and gut), while CQ studies offer much richer data. The authors did not provide their full array of equations utilized and their extrapolations to man do not cover the very long half-life known for HCQ (Tett et al, 1988).

Pharmacokinetics of Chloroquine in Man

The plasma concentration versus time courses of CQ in man for the 3 dose levels were well-captured with the PBPK model with 3 parameters needing customization (Figure 6, Table 4). These data are representative of many studies of CQ PK in man (Moore et al, 2011). Multiplying the rat *Kp* values by the man-to-rat *Vss* ratio of 7 was key. In turn, this implies that the total tissue and lysosomal concentrations of CQ are 7-fold higher in man than rat (Figure 7). This is supported by measurements of CQ showing skin-to-plasma ratios of about 34 at 48 hour after an IV dose in patients (Olatunde, 1971), while the 10-h skin ratio was 5.77 in rats (Table 2). Another cationic anti-malarial quinoline, HCQ, exhibits a *Vss* value that is 5.7-fold higher in man (86 L/kg) than in rats (15 L/kg) based on blood concentrations (Tett et al, 1988; Emami et al, 1998). It is possible that lysosomal pH is lower in man to produce greater sequestration of these drugs. Larger lysosomal volumes and greater acidic phospholipid content may be contributory.

JPET Fast Forward. Published on December 4, 2020 as DOI: 10.1124/jpet.120.000385
This article has not been copyedited and formatted. The final version may differ from this version.

On the other hand, *Vss* values for 10 other basic drugs are similar in man and rat (Sawada et al, 1984).

Therapeutic Implications of the PBPK Model

There are many therapeutic dosing regimens for CQ typically ranging 100 to 600 mg per day (Browning, 2014). The human data in Figure 6 reflects this range. The mechanism of action of CQ in malaria is thought to be its lysosomotropic effect on the acidic food vacuoles of the parasite increasing pH and interfering with the digestive degradation of hemoglobin in RBC.

Drugs such as CQ and HCQ are also used for treatment of patients with rheumatoid arthritis (RA) and systemic lupus erythematosus (SLE). Their myriad effects are attributed to interference of antigen processing in macrophages, down-regulation of immune responses, alteration of signaling pathways and transcriptional activity, and inhibition of cytokine production (Fox, 1993; Schrezenmeier and Dorner, 2020). While the lysosomotropic effects of CQ are stated to be most important clinically, more than 20 additional actions contributing to both therapeutic and adverse effects have been cited (Browning, 2014). There is current interest in using HCQ for autophagy modulation, the natural metabolic digestion of cell proteins and other materials in lysosomes; up-regulation of this process is a resistance mechanism for some tumors (Shi et al, 2017).

Our PK modeling predicts that CQ concentrations in the cytosol will be very low, similar to free drug concentrations in plasma and IS (Figures 4 and 7). However, multiple actions of CQ appear connected to or are triggered by the changes in lysosomal pH and associated alterations in lysosomal and cellular functions that ensue. The pharmacology of CQ and other lysosomotropic drugs is far more complex than can be explained by the very low unbound concentrations that are commonly thought to drive actions of many drugs. Some in vitro screening systems for drug

JPET Fast Forward. Published on December 4, 2020 as DOI: 10.1124/jpet.120.000385
This article has not been copyedited and formatted. The final version may differ from this version.

activity may not invoke the same lysosomal triggers. For example, the IC_{50} for CQ inhibition of mitogen-induced human lymphocyte proliferation is 19.5 µM or about 6.4 µg/mL (Kamal and Jusko, 2004), an in vitro system that is meaningful for immune effects of corticosteroids. This concentration is far above peak exposures of 0.1 µg/mL after 600 mg doses of CQ (Figure 6). Yet CQ is effective at these doses for treatment of patients with RA and SLE.

Of current interest, CQ and HCQ were found active in inhibiting SARS-CoV-2 in vitro with IC_{50} concentrations of around 6 µM (Liu et al, 2020). These too are well above typical therapeutic plasma concentrations. It can be questioned whether these in vitro responses are relevant in vivo and whether a lysosomotropic mechanism is present in some cell cultures. It has been argued that the lysosomotropic effects could partly make CQ effective as an anti-viral agent (Savarino et al, 2003; Plantone and Koudriavtseva, 2018). Some viruses enter their target cells by endosomes that merge into lysosomes. The low pH and action of enzymes liberates infectious nucleic acids from virus particles. Raising the lysosomal pH thus interferes with this process. However, recent attempts to use CQ and HCQ to treat COVID-19 viral infections have not shown efficacy and risk various toxicities (Qaseem et al, 2020).

This report demonstrates application of state-of-the-art PBPK modeling concepts, methods, and insights for an old drug with highly interesting tissue distribution and mechanisms of action. The principles underlying this modeling approach will likely be relevant to other cationic drugs that sequester in lysosomes, although their physicochemical properties and degree of changes in lysosome pH and structure may require more specific adjustments.

Acknowledgments

JPET Fast Forward. Published on December 4, 2020 as DOI: 10.1124/jpet.120.000385
This article has not been copyedited and formatted. The final version may differ from this version.

We appreciate the review of this manuscript by Dr. Viera Lucakova from SimulationsPlus.

Authorship Contributions

Participated in research design: Liu and Jusko

Conducted experiments: Not applicable.

Performed data analysis: Liu

Wrote or contributed to the writing of the manuscript: Liu and Jusko

References

Adelusi SA and Salako LA (1982a) Kinetics of the distribution and elimination of chloroquine in the rat. *Gen Pharmacol* 13:433-437.

Adalusi SA and Salako LA (1982b). The effect of protein-energy malnutrition on the absorption, distribution and elimination of chloroquine in the rat. *General Pharmacol* 13: 505–509.

Allison AC and Young MR (1964) Uptake of dyes by living cells in culture, Life Sciences 3:1407-1414.

Assmus F, Houston JB and Galetin A (2017) Incorporation of lysosomal sequestration in the mechanistic model for prediction of tissue distribution of basic drugs. *Eur J Pharm Sci* 109:419-430.

Berezhkovskiy LM (2004) Volume of distribution at steady state for a linear pharmacokinetic system with peripheral elimination. *J Pharm Sci* 93:1628-1640.

Bernareggi A and Rowland M (1991) Physiologic modeling of cyclosporin kinetics in rat and man. *J Pharmacokinet Biopharm* 19:21-50.

Brown RP, Delp MD, Lindstedt SL, Rhomberg LR and Beliles RP (1997) Physiological parameter values for physiologically based pharmacokinetic models. *Toxicol Ind Health* 13:407-484.

Browning DJ (2014) Pharmacology of Chloroquine and Hydroxychloroquine. In: Hydroxychloroquine and Chloroquine Retinopathy. Springer, New York, NY. https://doi.org/10.1007/978-1-4939-0597-3_2.

Collins KP, Jackson KM, and Gustafson DL (2018) Hydroxychloroquine: A physiologically-based pharmacokinetic model in the context of cancer-related autophagy modulation, *J Pharmacol Exp Ther* 365: 447-459.

Cramb G (1986) Selective lysosomal uptake and accumulation of the beta-adrenergic antagonist propranolol in cultured and isolated cell systems. *Biochem Pharmacol* 35: 1365-1372.

Davies B and Morris T (1993) Physiological parameters in laboratory animals and humans. *Pharm Res*. 10(7):1093-5

Daniel M. Syrek M, Janczar L and Boksa J (1995) The pharmacokinetics of promazine and its metabolites after acute and chronic administration to rats - A comparison with the pharmacokinetics of imipramine. *Pol J Pharmacol*. 47: 127-136.

Ducharme J and Farinotti R (1996) Clinical pharmacokinetics and metabolism of chloroquine: Focus on recent developments. *Clinical Pharmacokin* 31: 257-274.

Emami J, Pasutto FM and Jamali F (1998) Effect of experimental diabetes mellitus and arthritis on the pharmacokinetics of hydroxychloroquine enantiomers in rats. *Pharm Res* 15:897-903.

Feke GT, Tagawa H, Deupree DM, Goger DG, Sebag J, and Weiter JJ (1989) Blood flow to the normal human retina. *Invest Ophthamol Vis Sci* 30: 58-65.

Fox RJ (1993) Mechanism of action of hydroxychloroquine as an antirheumatic drug, *Sem Arthritis Rheumatism*. 23: 82-91.

Frisk-Holmberg M, Bergqvist Y, Termond E and Domeij-Nyberg B (1984) The single dose kinetics of chloroquine and its major metabolite desethylchloroquine in healthy subjects. *Eur J Clin Pharmacol* 26:521-530.

(2019) GastroPlus Manual, Simulations Plus, Inc, 42505 10th Street West, Lancaster, California.

Geng Y, Greenberg KP, Wolfe R, Gray DC, Hunter JJ, Dubra A, Flannery JG, Williams DR and Porter J (2009) In vivo imaging of microscopic structures in the rat retina. *Invest Ophthalmol Vis Sci* 50:5872-5879.

Grundmann M, Mikulikrova I and Vrublovsky P (1972) Tissue distribution of chloroquine in rats in the course of long-term application. *Arch Int Pharmacodyn Ther* 197:45-52.

Hostetler KY, Reasor M, and Yazaki PJ (1985) Chloroquine-induced phospholipid fatty liver. Measurement of drug and lipid concentrations in rat liver lysosomes, *J Biol Chem* 260: 215-219.

Huang W and Isoherranen N (2020) Sampling site has a critical impact on physiologically based pharmacokinetic modeling, J Pharmacol Exp Ther 372: 30-45.

Ishida Y, Nayak S, Mindell JA and Grabe M (2013) A model of lysosomal pH regulation. *J Gen Physiol* 141:705-720.

Ishizaki J, Yokogawa K, Ichimura F, and Ohkuma S (2000) Uptake of imipramine in rat liver lysosomes in vitro and its inhibition by basic drugs, *J Pharmacol Exp Ther* 294: 1088 – 1098.

Jeong Y-S, Yin C-S, Ryu H-M, Noh C-K, Song Y-K, and Chung S-J (2017) Estimation of the minimun permeability coefficient in rats for perfusion-limited tissue distribution in whole-body physiologically-based pharmacokinetics, Eur J Pharmaceut Biopharm 115: 1-17.

Kamal MA and Jusko WJ (2004) Interactions of prednisolone and other immunosuppressants used in dual treatment of systemic lupus erythematosus in lymphocyte proliferation assays. J Clin Pharmacol, 44:1034-45.

Kim K-A, Park J-Y, Lee J-S, and Lim S (2003) Cytochrome P-450 2C8 and CYP3A4/5 are involved in chloroquine metabolism in human liver microsomes, *Arch Pharm Res* 26: 631-637.

Lee HB and Blaufox MD (1985) Blood volume in the rat. J Nucl Med 26:72-76.

Liu J, Cao R, Xu M, Wang X, Zhang H, Hu H, Li Y, Hu Z, Zhang W, and Wang M (2020) Hydroxychloroquine, a less toxic derivative of chloroquine, is effective in inhibiting SARS-CoV-2 infection in vitro, *Cell Discovery* 6:16.

Lullman H and Wehling M (1979) The binding of drugs to different polar lipids in vitro, *Biochem Pharmacol* 28: 3409-3415.

MacIntyre AC and Cutler DJ (1988) Role of lysosomes in hepatic accumulation of chloroquine, *J Pharm Sci* 77: 196-199.

MacIntyre AC and Cutler DJ (1993) Kinetics of chloroquine uptake into isolated rat hepatocytes, *J Pharm Sci* 82: 592-600.

McChesny EW, Banks WF, and Sullivan DJ (1965) Metabolism of chloroquine and hydroxychloroquine in albino and pigmented rats, *Toxicol Appl Pharmacol* 7: 627-636.

McChesney EW, Conway WD, Banks WF, Rogers JE, Shekosky JM, Grace AJ, Jensen AF and Sullivan DJ (1966) Studies of the metabolism of some compounds of the 4-amino-7-chloroquinoline series. *J Pharmacol Exp Ther* 151:482-493.

McChesny EQ, Banks WF, and Fabian RJ (1967) Tissue distribution of chloroquine, hydroxychloroquine, and desethylchloroquine in the rat, Toxicol Appl Pharmacol 10: 501-513.

Moore BR, Page-Sharp M, Stoney JR, Bett KF, Jago JD, and Batty KT (2011) Pharmacokinetics, pharmacodynamics, and allometric scaling of chloroquine in a murine malaria model, *Antimicrob Ag Chemother* 55: 3899 – 3907.

Myers BM, Tietz PS, Tarara JE, and LaRusso NF (1995) Dynamic measurements of the acute and chronic effects of lysosomotropic agents on hepatocyte lysosomal pH using flow cytometry, *Hepatology* 22: 1519-1526.

Olatunde IA (1971) Chloroquine concentrations in the skin of rabbits and man. *Br J Pharmacol* 43:335-340.

Osifo NG (1980) Chloroquine pharmacokinetics in tissues of pyrogen treated rats and implications for chloroquine related pruritus, *Res Commun Chem Path Pharmacol* 30: 419-430.

Plantone D and Koudriavtseva T (2018) Current and future use of chloroquine and hydroxychloroquine in infectious, immune, neoplastic, and neurological diseases: A mini-review. Clin Drug Investig. 38:653-671.

Poulin P and Theil FP (2002) Prediction of pharmacokinetics prior to in vivo studies. 1. Mechanism-based prediction of volume of distribution. *J Pharm Sci* 91:129-156.

Qaseem A, Yost J, Etxeandia-Ikobaltzeta I, et al, on behalf of the Scientific Medical Policy Committee of the American College of Physicians (2020) Should clinicians use chloroquine or hydroxychloroquine alone or in combination with azithromycin for the prophylaxis or treatment of COVID-19? Living practice points from the American College of Physicians (Version 1), Ann Intern Med 173: 137-143.

Rodgers T, Leahy D, and Rowland M (2005) Physiologically based pharmacokinetic modeling 1: Predicting the tissue distribution of moderate-to-strong bases, *J Pharm Sci* 94: `259-276.

Rodgers T and Rowland M (2006) Physiologically based pharmacokinetic modelling 2: Predicting the tissue distribution of acids, very weak bases, neutrals and zwitterions. *J Pharm Sci* 95:1238-1257.

Rodionov N, Graph Digitizer, Version 1.9.2000 (http://geocities.com/graph digitizer/).

Savarino A, Boelaert JR, Cassone A, Majori G, and Cauda R (2003) Effects of chloroquine on viral infections: An old drug against today's diseases? *The Lancet Infectious Diseases* 3: 722-727.

Sawada Y, Hanano M, Sugiyama Y, Harashima H and Iga T (1984) Prediction of the volumes of distribution of basic drugs in humans based on data from animals. *J Pharmacokinet Biopharm* 12:587-596.

Schrezenmeier E and Dorner T (2020), Mechanisms of action of hydroxychloroquine and chloroquine: Implications for rheumatology, *Nature Reviews Rheumatology* 16: 155-166.

Schmitt MV, Lienau P, Fricker G, and Reichel A (2019), Quantitation of lysosomal trapping of basic lipophilic compounds using in vitro assays and in silico predictions based on the determination of the full pH profile of the endo-/lysosomal system in rat hepatocytes, *Drug Met Dispos* 47: 49-57.

Schroeder RL and Gerber JP (2014) Chloroquine and hydroxychloroquine binding to melanin: Some possible consequences for pathologies, *Toxicol Rep* 1: 963-968.

Shi TT, Yu XX, Yan LJ, and Xiao HT (2017) Research progress of hydroxychloroquine and autophagy inhibitors on cancer, *Cancer Chemother Pharmacol* 79:287-294.

Tett SE, Cutler DJ, Day RO, and Brown KF (1988) A dose-ranging study of the pharmacokinetics of hydroxychloroquine following intravenous administration to healthy volunteers, *Br J Clin Pharmacol* 26, 303-313.

Tietz PS, Yamazaki K, and LaRusso NF (1990) Time-dependent effects of chloroquine on pH of hepatocyte lysosomes, *Biochem Pharmacol* 40: 1419-1421.

Trapp S, Rosania GR, Horobin RW and Kornhuber J (2008) Quantitative modeling of selective lysosomal targeting for drug design. *Eur Biophys J* 37:1317-1328.

Walker O, Birkett DJ, Alvan G, Gustafsson LL, and Sjoqvist F, (1983) Characterization of chloroquine plasma protein binding in man, *Br J Clin Pharmac* 15: 375-377.

Watanabi and Kozaki A (1978) Relationship between partition coefficient and apparent volumes of distribution for basic drugs. I, *Chem Pharm Bull* 26: 665-667.

White NJ, (1985) Clinical pharmacokinetics of antimalarial drugs. *Clin Pharmacokinet* 10, 187–215.

Yokogawa K, Ishizki J, Ohkuma S, and Miyamoto K, (2002) Influence of lipophilicity and lysosomal accumulation in tissue distribution kinetics of basic drugs: A physiologically based pharmacokinetic model, *Methods Find Exp Clin Pharmacol* 24: 81-93.

Yu DY, Alder VA and Cringle SJ (1991) Measurement of blood flow in rat eyes by hydrogen clearance. *Am J Physiol* 261:H960-968.

Zheng N, Zhang X, and Rosania GR (2011) Effect of phospholipidosis on the cellular pharmacokinetics of chloroquine, *J Pharmacol Exp Ther* 336: 661-67.

Footnotes

This work was supported by NIH Grant R35 GM131800.

No author has an actual or perceived conflict of interest with the contents of this article.

This article has Supplemental Materials available at jpet.aspetjournals.org.

JPET Fast Forward. Published on December 4, 2020 as DOI: 10.1124/jpet.120.000385
This article has not been copyedited and formatted. The final version may differ from this version.

Legends to Figures

Figure 1. Schematic of the PBPK model structure for chloroquine. Parameters and symbols are defined in the text and tables. Lines with arrows indicate plasma flows and drug transport and elimination.

Figure 2. Schematic of lysosomal distribution model structure for chloroquine. Parameters and symbols are defined in the text and tables. Lines with arrows indicate plasma flows and drug transfer. The lysosome model was applied to all tissues except eye and remainder.

Figure 3. Chloroquine concentration-time profiles for all tissues after 10 mg/kg IP single-dosing in rats. Measured chloroquine concentrations in plasma, red blood cells (RBC) and tissues are indicated by different symbols and black solid lines show the PBPK model fitting. Data are from (Adelusi and Salako, 1982a).

Figure 4. Model-predicted lysosome, cytosol, interstitial space (IS), neutral lipid (NL), neutral phospholipid (NP), and acidic phospholipid (AP) chloroquine concentrations versus time after 10 mg/kg IP dosing in rats. Solid symbols are observed values and black lines are PBPK-fitted total tissue concentrations.

Figure 5. Model-predicted lysosome pH values versus time in indicated tissues after 10 mg/kg IP dosing in rats. Broken line indicates the expected initial rise caused by influx of drug, and dot-dash line indicates the presumed lysosomal baseline and steady-state pH.

Figure 6. Plasma concentration-time profiles of chloroquine after single oral dosing in healthy humans. Black lines show the PBPK model fitting. Data were digitized from (Frisk-Holmberg et al, 1984).

Figure 7. Model-predicted lysosome, cytosol, interstitial space (IS), neutral lipid (NL), neutral phospholipid (NP), and acidic phospholipids (AP) chloroquine concentrations versus time in four indicated tissues after 600 mg oral dosing in man.

JPET Fast Forward. Published on December 4, 2020 as DOI: 10.1124/jpet.120.000385
This article has not been copyedited and formatted. The final version may differ from this version.

Table 1. Physiological parameters of tissues for chloroquine in rat and man

Tissue		Volume (*V*, mL/kg)		Plasma Flow (*Q*, mL/h/kg)		Fractional Interstitial Space (%) [d]
		Rat [a, b]	*Man* [b]	*Rat* [b]	*Man* [b]	
Liver		32.3	25.7	2191	628.6	16.1
Kidney		5.25	4.45	1385	484.6	27.3
Lung		2.64	7.60	11181 [c]	2769	33.6
Spleen		0.973	2.60	679	138.6	20.7
Heart		2.19	4.71	574	110.7	32.0
Brain		4.64	20.1	248	315.7	16.2
Muscle		422.7	400	3512	528.9	11.8
Skin		174.5	37.1	758	160.6	38.2
Eye		0.74 [c]	0.214 [c]	99.6 [c]	0.073 [c]	-
Blood		105.3	79.1	18641	4615	-
Plasma	Artery	21.1	13.7	11185 [c]	2769 [c]	-
	Vein	42.1	32.1	11185 [c]	2769 [c]	-
Remainder		290.9	452.1	1735	401	-
GFR (mL/h/kg) [e]	*Rat*	315				
	Man	111				

[a] Corrected for residual blood volume (Bernareggi and Rowland, 1991)

[b] From (Brown et al, 1997)

[c] From (Feke et al, 1989), (Yu et al, 1991), and (Geng et al, 2009)

[d] From (Rodgers et al, 2005)

[e] From (Davies B and Morris T et al, 1993)

Table 2. Summary of fitted and observed chloroquine pharmacokinetic parameters for rat (CV%)

Tissue	B_{max} (µg/mL)	K_D (µg/mL)	*PS* (mL/h/kg)	C_{tissue}/C_{plasma}			Estimated *Kp* [a] by GastroPlus™			
				10 h	50 h	150 h	Method 1	Method 2	Method 3	Method 4
Liver	36.8 (71.9)	K_{D1}: 0.00452 (17.7)	PS_1:7297 (43.2)	150	318	634	7.10	10.0	376	858
Kidney	14.2 (12.3)	K_{D1}: 0.00452 (17.7)	PS_2:269 (18.6)	81.8	182	421	4.26	6.04	403	750
Lung	15.6 (9.31)	K_{D1}: 0.00452 (17.7)	PS_2:269 (18.6)	129	275	625	8.44	14.7	319	597
Spleen	12.9 (8.58)	K_{D1}: 0.00452 (17.7)	PS_2:269 (18.6)	131	267	589	4.34	9.16	255	403
Heart	3.78 (8.68)	K_{D1}: 0.00452 (17.7)	PS_3:148 (29.9)	32.4	65.6	143	4.75	6.73	181	261
Brain	1.74 (8.89)	K_{D1}: 0.00452 (17.7)	PS_3:148 (29.9)	19.0	38.4	84.5	11.3	16.1	35.6	40.2
Muscle	0.525 (10.9)	K_{D2}: 0.00544 (21.8)	PS_4: 3798 (35.2)	6.32	12.0	23.9	4.33	6.14	124	165
Skin	0.695 (10.6)	K_{D2}: 0.00544 (21.8)	PS_4: 3798 (35.2)	5.77	10.9	21.4	5.29	7.50	107	139
Eye	1.49 (9.55)	K_{D2}: 0.00544 (21.8)	-	19.4	35.6	74.5	NA	NA	NA	NA
Remainder	7.04 (30.8)	K_{D1}: 0.00452 (17.7)	-		-	-	NA	NA	NA	NA
K_b			RBC to plasma partition coefficient of RBC						11.6 (10.8)	
ka_{liver}			Absorption rate constant into liver (h^{-1})						0.0306 (9.40)	
ka_{plasma}			Absorption rate constant into plasma (h^{-1})						0.372 (20.6)	
$CL_{u,int}$			Hepatic intrinsic clearance (mL/h/kg)						11600 (70.3)	
$CL_{s,renal}$			Systemic renal clearance (mL/h/kg)						630 [b]	
fu			Free fraction of drug in plasma (%)						40.0 [c]	

[a] Estimated partition coefficient (*Kp*) value using GastroPlus: Method 1, (Poulin and Theil, 2002); 2, (Berezhkovskiy, 2004); 3, (Rodgers and Rowland, 2006); 4, (SimulationsPlus).

[b] Fixed to 2-fold GFR

[c] From (Ducharme and Farinotti, 1996)

JPET Fast Forward. Published on December 4, 2020 as DOI: 10.1124/jpet.120.000385
This article has not been copyedited and formatted. The final version may differ from this version.

Table 3. Summary of parameters for lysosome distribution model

Tissue	Lysosome volume (%) [a]	Component fraction (%) [b]							
		Interstitial Space	Cytosol		Neutral Lipid		Neutral Phospholipid		AP (mg/g) [c]	
			Rat	*Man*	*Rat*	*Man*	*Rat*	*Man*	*Rat*	*Man*
Liver	9.55	16.1	57.3	59.0	1.40	3.48	2.40	2.52	4.56	4.56
Kidney	3.28	27.3	48.3	51.0	1.20	2.07	2.42	1.62	5.03	5.03
Lung	2.77	33.6	44.6	47.5	2.20	0.30	1.28	0.80	3.91	3.91
Spleen	3.18	20.7	57.9	58.1	0.77	0.20	1.13	1.98	3.18	3.18
Heart	0.595	32.0	45.6	45.0	1.40	1.15	1.11	1.66	2.25	2.25
Brain	0.481	16.2	62.0	60.8	3.90	5.10	0.15	5.65	0.40	9.60
Muscle	0.126	11.8	63.0	64.2	1.00	2.38	0.72	0.72	1.53	1.53
Skin	0.096	38.2	29.1	33.6	6.00	2.84	0.44	1.11	3.18	3.18
RBC	-	-	60.3		0.17		0.29		0.50	
pKa1					10.1					
pKa2					8.40					
LogP					4.63					
pH [d]	Lysosome				5.0 (at 10 h)					
	Cytosol				7.0					
	IS and Plasma				7.4					
Fn	Lysosome				3.16E-09 (at 10 h)					
	Cytosol				3.04E-05					
	IS and Plasma				1.81E-04					

[a] Calculated based on 10 h fitted data

[b] From (Rodgers et al, 2005) and (Poulin and Theil, 2002).

[c] AP (acidic phospholipid concentration)

[d] From (Assmus et al, 2017)

JPET Fast Forward. Published on December 4, 2020 as DOI: 10.1124/jpet.120.000385
This article has not been copyedited and formatted. The final version may differ from this version.

Table 4. Summary of assigned and fitted chloroquine pharmacokinetic parameters for man (CV%)

Parameter	Description	Estimated value
$CL_{u,int}$	Hepatic clearance (mL/h/kg)	1060 (14.5)
ka_{oral}	Absorption rate constant (h^{-1})	0.0245 (13.2)
K_{D1}	Dissociation constant (μg/ml)	0.0228 (8.5)
R	Adjustment factor for *Kp*	7.0 [a]
F	Bioavailability (%)	100 [b]
fu	Free fraction of drug in plasma (%)	40.0 [c]

[a] Based on multiplying PBPK Kp_{tissue} values by the ratio of man-to-rat V_{ss}.

[b] From (Frisk-Holmberg et al, 1984)

[c] From (Ducharme and Farinotti, 1996)

JPET Fast Forward. Published on December 4, 2020 as DOI: 10.1124/jpet.120.000385
This article has not been copyedited and formatted. The final version may differ from this version.

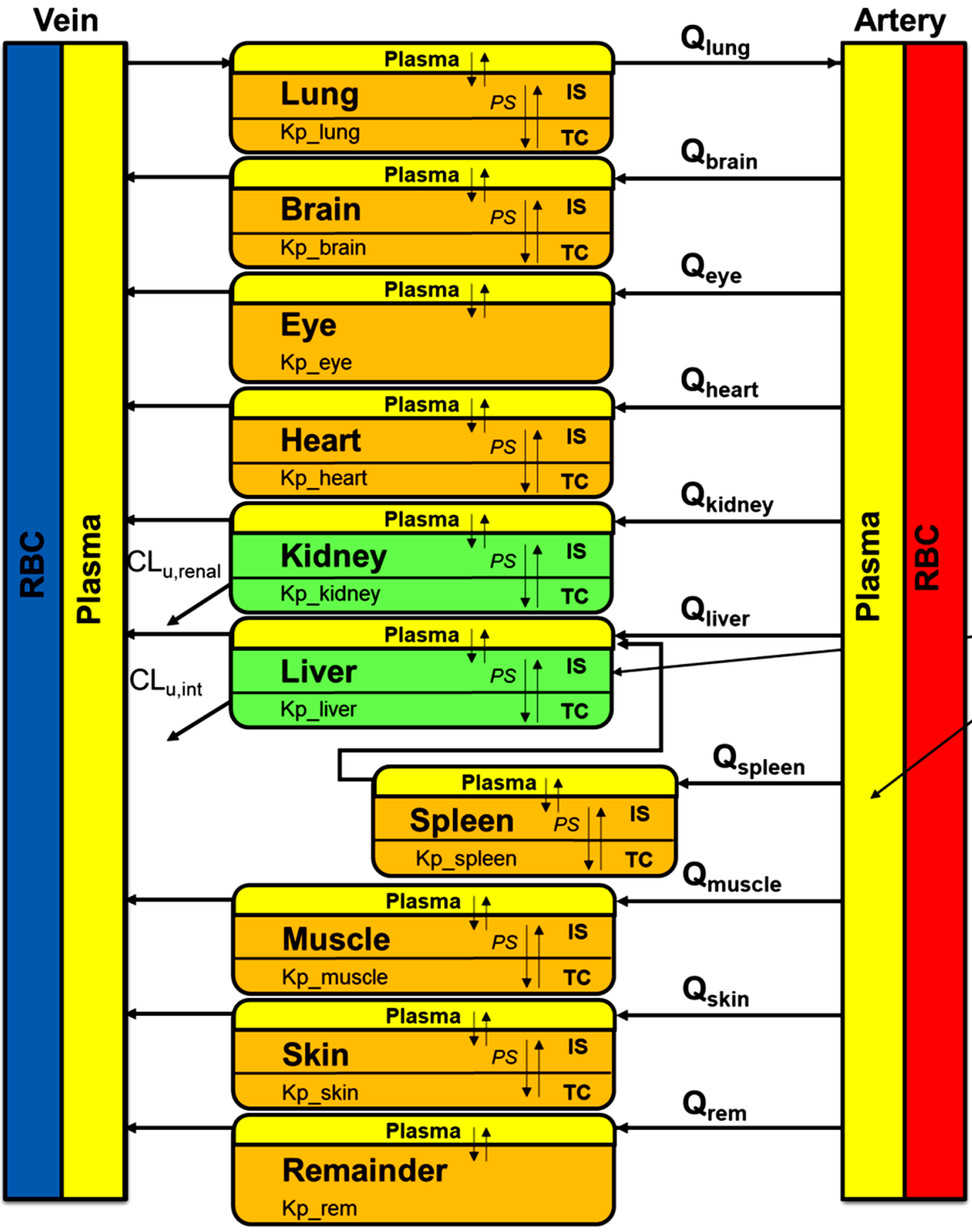

Figure 1

JPET Fast Forward. Published on December 4, 2020 as DOI: 10.1124/jpet.120.000385
This article has not been copyedited and formatted. The final version may differ from this version.

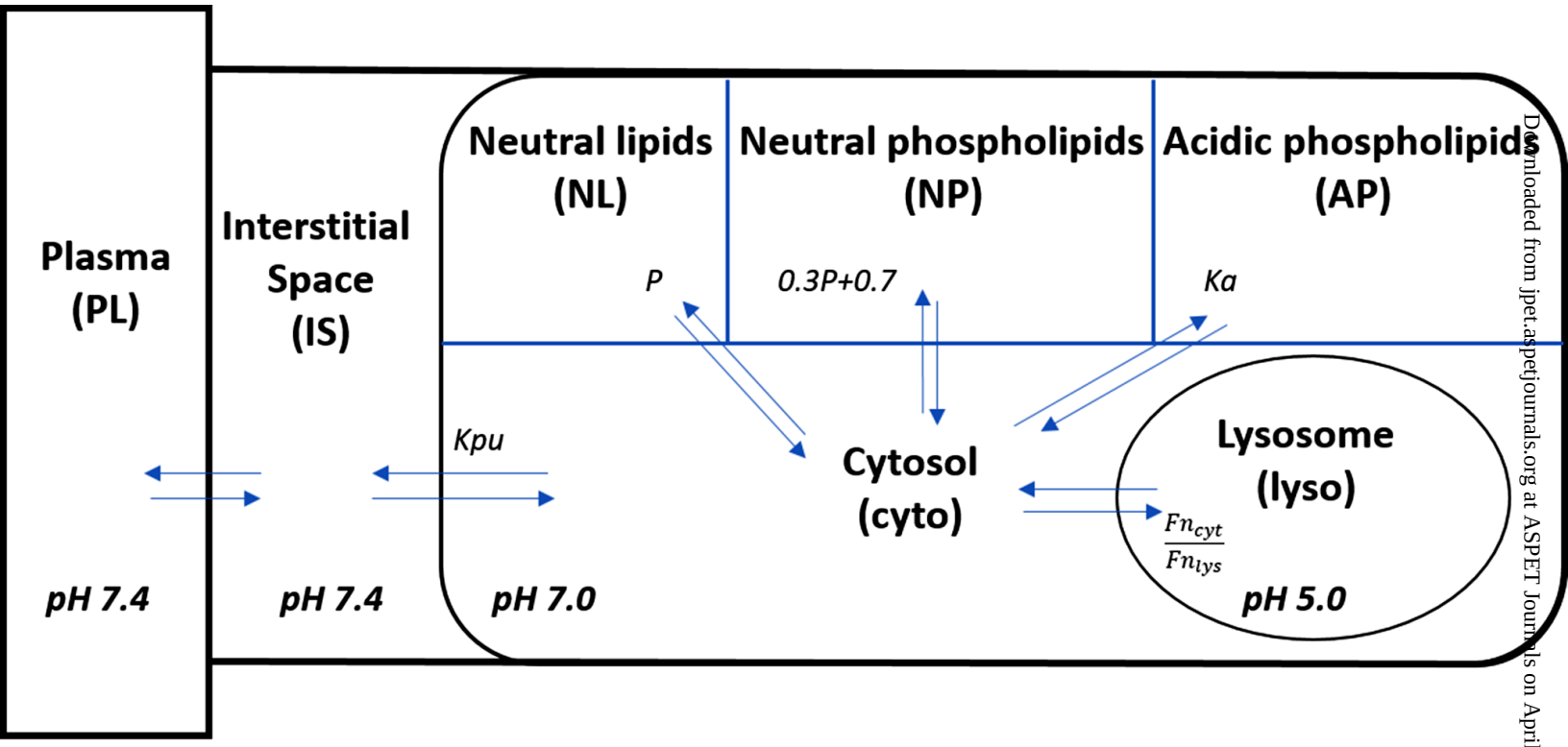

Figure 2

JPET Fast Forward. Published on December 4, 2020 as DOI: 10.1124/jpet.120.000385
This article has not been copyedited and formatted. The final version may differ from this version.

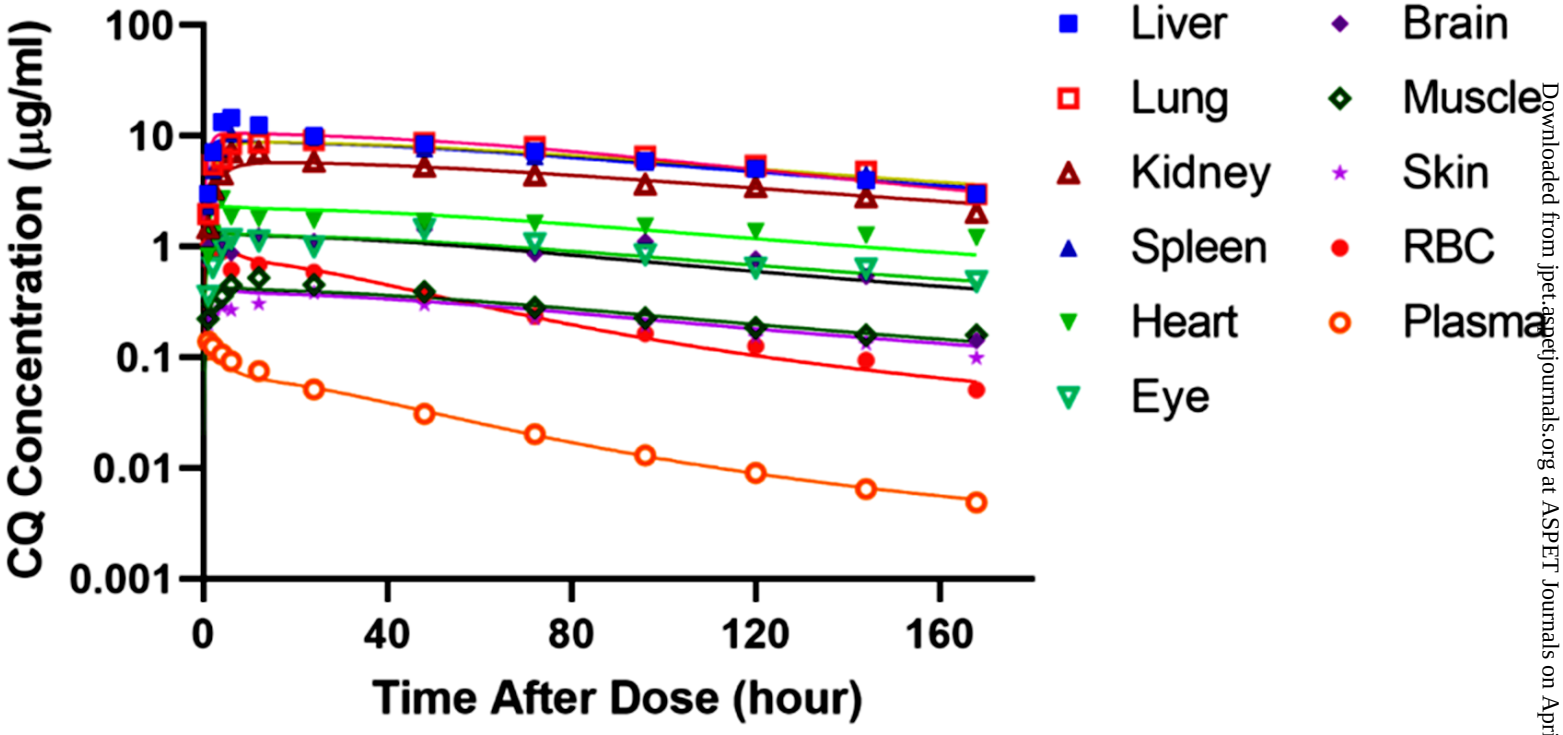

Figure 3

JPET Fast Forward. Published on December 4, 2020 as DOI: 10.1124/jpet.120.000385
This article has not been copyedited and formatted. The final version may differ from this version.

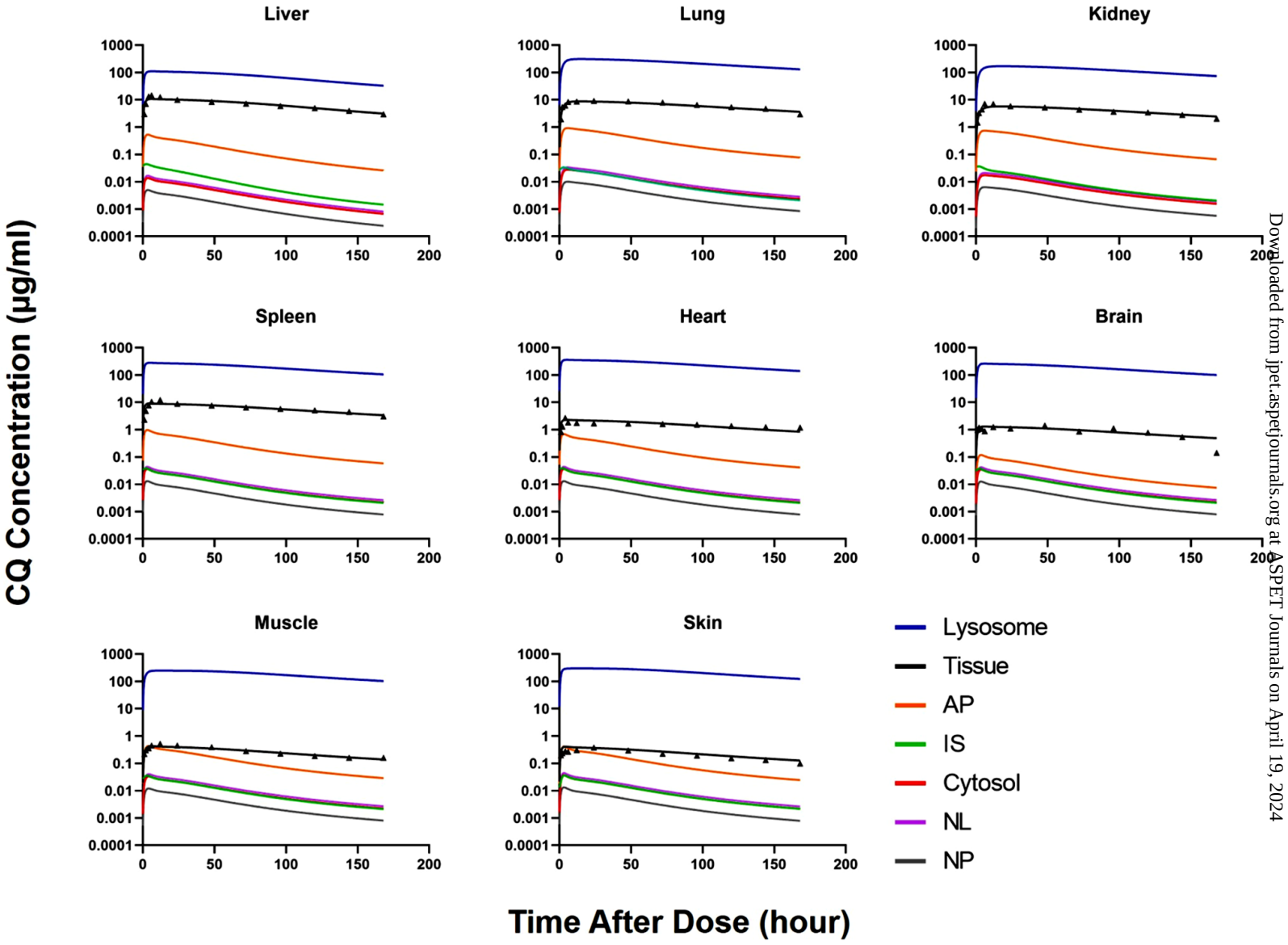

Figure 4

JPET Fast Forward. Published on December 4, 2020 as DOI: 10.1124/jpet.120.000385
This article has not been copyedited and formatted. The final version may differ from this version.

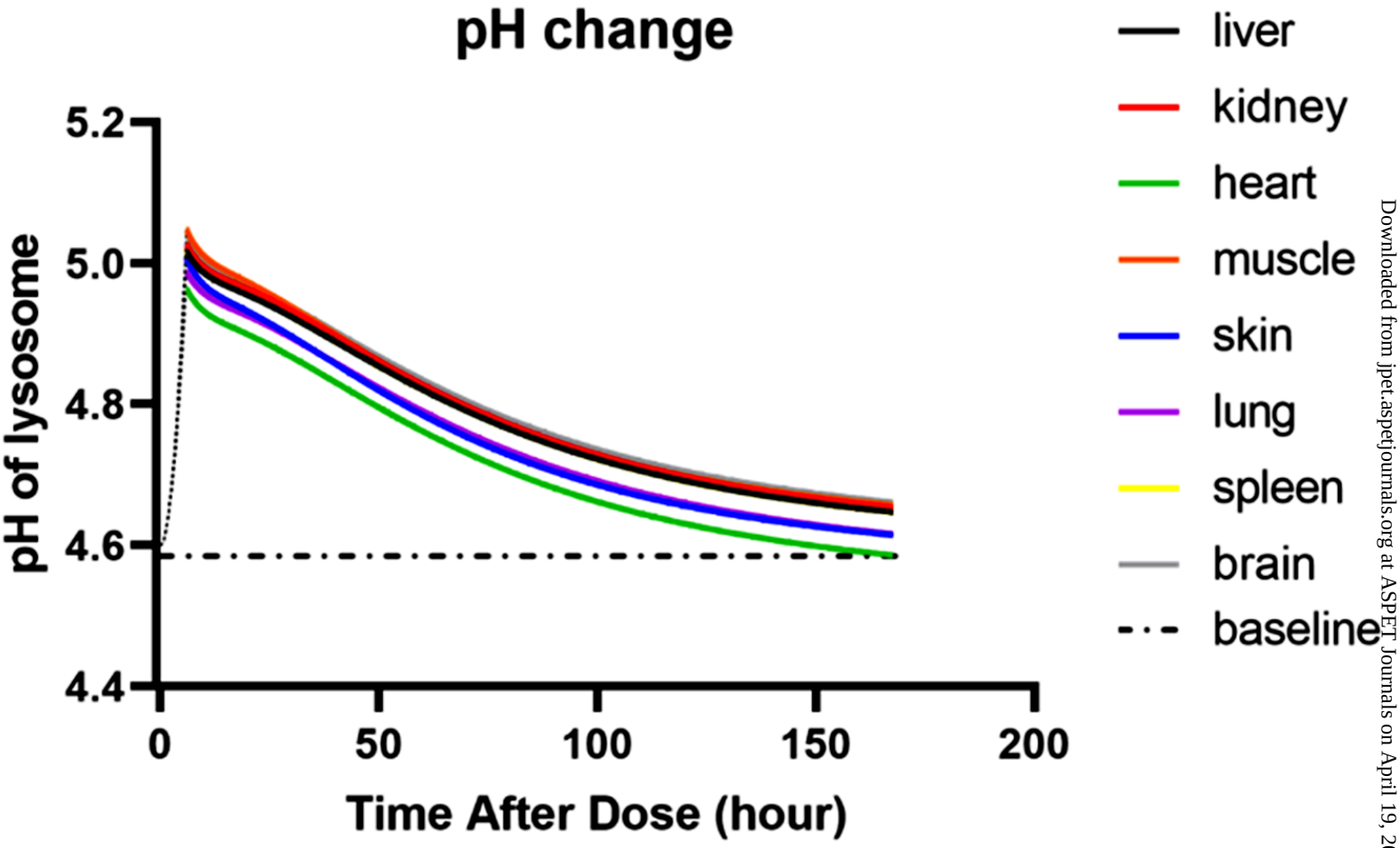

Figure 5

JPET Fast Forward. Published on December 4, 2020 as DOI: 10.1124/jpet.120.000385
This article has not been copyedited and formatted. The final version may differ from this version.

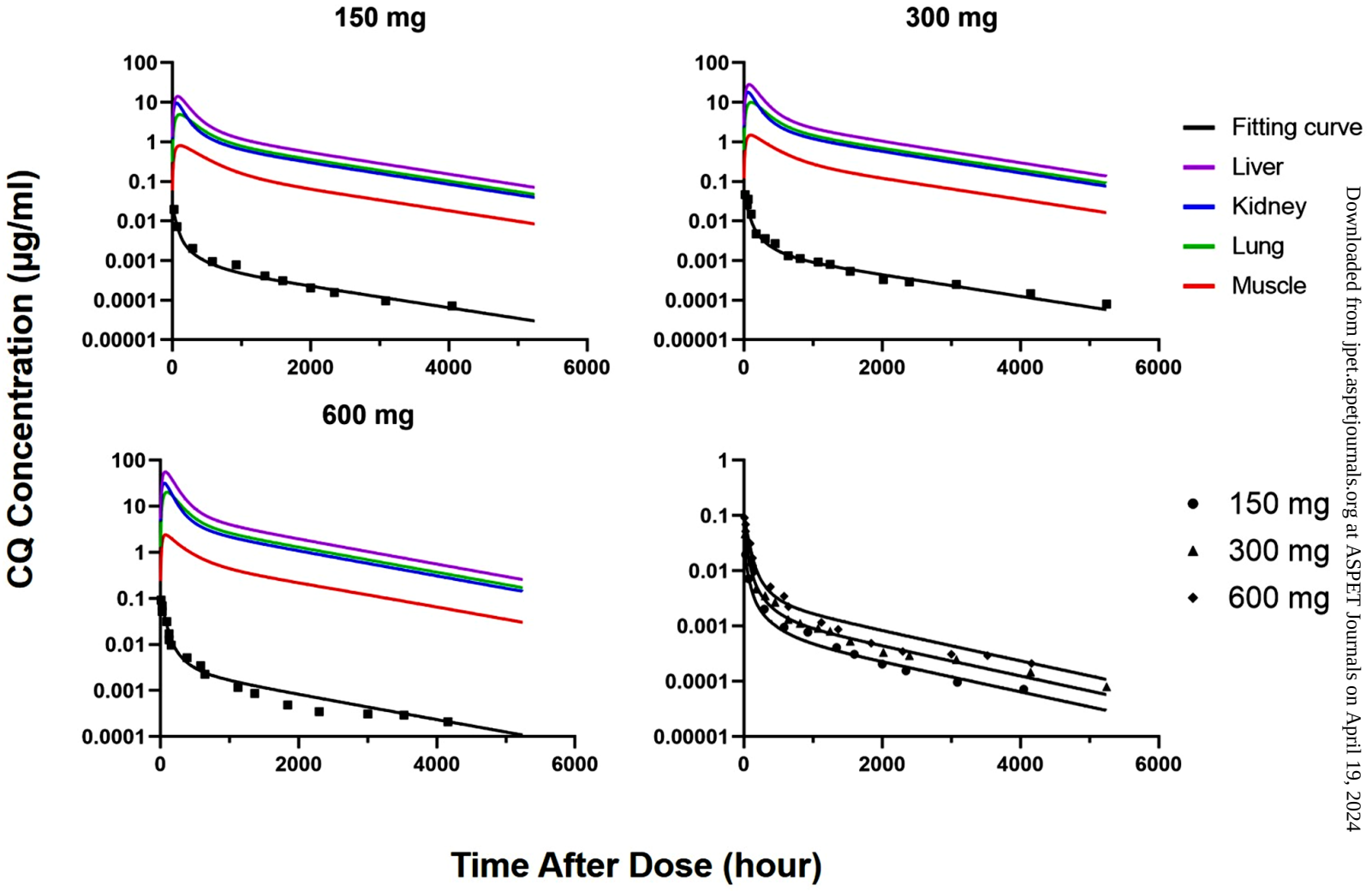

Figure 6

JPET Fast Forward. Published on December 4, 2020 as DOI: 10.1124/jpet.120.000385
This article has not been copyedited and formatted. The final version may differ from this version.

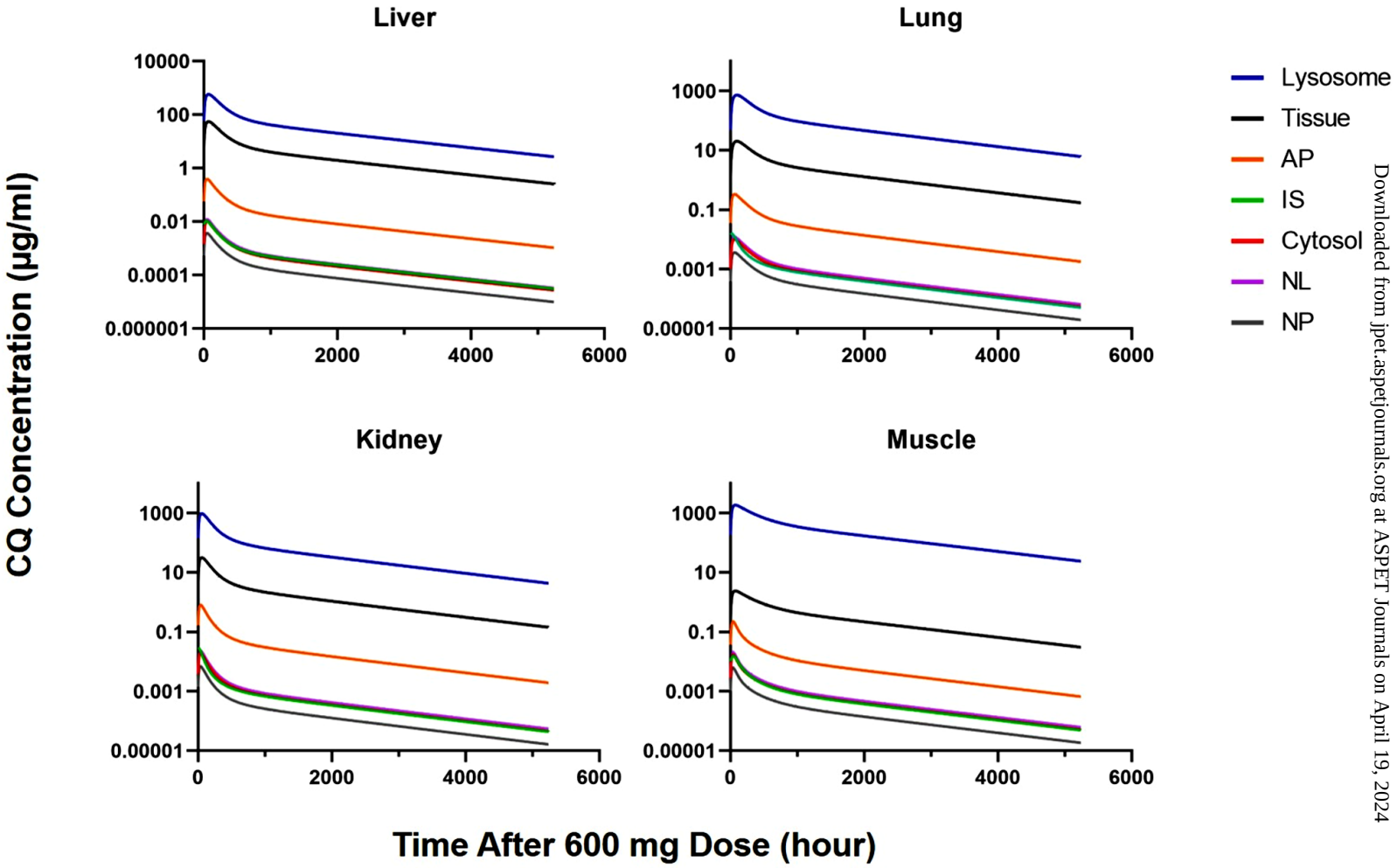

Figure 7